

RESEARCH ARTICLE

10.1002/2016JC012643

Key Points:

- Typhoon Wutip generated significant changes in oceanographic conditions in the surface mixed layer over the northern South China Sea
- Wutip enhanced the $p\text{CO}_{2\text{sea}}$ in the cyclonic eddy and surrounding water and decreased the $p\text{CO}_{2\text{sea}}$ in the anticyclonic eddy water
- The noticeable spatial variation in $p\text{CO}_{2\text{sea}}$ was affected mainly by the storm-induced mixing and associated changes in stratifications

Correspondence to:

D. L. Tang,
lingzistdl@126.com

Citation:

Ye, H., J. Sheng, D. Tang, E. Siswanto, M. Ali Kalhoro, and Y. Sui (2017), Storm-induced changes in $p\text{CO}_2$ at the sea surface over the northern South China Sea during Typhoon Wutip, *J. Geophys. Res. Oceans*, 122, doi:10.1002/2016JC012643.

Received 24 DEC 2016

Accepted 4 MAY 2017

Accepted article online 12 MAY 2017

Storm-induced changes in $p\text{CO}_2$ at the sea surface over the northern South China Sea during Typhoon Wutip

Haijun Ye¹ , Jinyu Sheng^{1,2}, Danling Tang¹ , Eko Siswanto^{3,4} , Muhsan Ali Kalhoro^{1,5}, and Yi Sui^{1,2}

¹State Key Laboratory of Tropical Oceanography, South China Sea Institute of Oceanology, Chinese Academy of Sciences, Guangzhou, China, ²Department of Oceanography, Dalhousie University, Halifax, Nova Scotia, Canada, ³Department of Environmental and Geochemical Cycle Research, Japan Agency for Marine-Earth Science and Technology, Yokohama, Japan, ⁴Research and Development Center for Global Change, Japan Agency for Marine-Earth Science and Technology, Yokohama, Japan, ⁵Faculty of Marine Sciences, Lasbela University of Agriculture, Water and Marine Sciences, Uthal, Pakistan

Abstract In situ oceanographic measurements were made before and after the passage of Typhoon Wutip in September 2013 over the northern South China Sea. The surface geostrophic circulation over this region inferred from satellite altimetry data features a large-size anticyclonic eddy, a small-size cyclonic eddy, and smaller-size eddies during this period. Significant typhoon-induced changes occurred in the partial pressure of CO_2 at the sea surface ($p\text{CO}_{2\text{sea}}$) during Wutip. Before the passage of Wutip, $p\text{CO}_{2\text{sea}}$ was about 392.92 ± 1.83 , 390.31 ± 0.50 , and $393.04 \pm 4.31 \mu\text{atm}$ over the cyclonic eddy water, the anticyclonic eddy water, and areas outside two eddies, respectively. The entire study region showed a carbon source ($1.31 \pm 0.46 \text{ mmol CO}_2 \text{ m}^{-2} \text{ d}^{-1}$) before Wutip. In the cyclonic eddy water after Wutip, high sea surface salinity (SSS), low sea surface temperature (SST), and high $p\text{CO}_{2\text{sea}}$ ($413.05 \pm 7.56 \mu\text{atm}$) made this area to be a carbon source ($3.30 \pm 0.75 \text{ mmol CO}_2 \text{ m}^{-2} \text{ d}^{-1}$). In the anticyclonic eddy water after Wutip, both the SSS and SST were lower, $p\text{CO}_{2\text{sea}}$ was also lower ($383.03 \pm 3.72 \mu\text{atm}$), and this area became a carbon sink ($-0.11 \pm 0.55 \text{ mmol CO}_2 \text{ m}^{-2} \text{ d}^{-1}$), in comparison with the pretyphoon conditions. The typhoon-induced air-sea CO_2 flux reached about $0.03 \text{ mmol CO}_2 \text{ m}^{-2} \text{ d}^{-1}$. Noticeable spatial variations in $p\text{CO}_{2\text{sea}}$ were affected mainly by the typhoon-induced mixing/upwelling and vertical stratifications. This study suggests that the local air-sea CO_2 flux in the study region was affected significantly by oceanographic conditions during the typhoon.

1. Introduction

Many climate models predicted that the intensity of the strongest tropical cyclones over the southern Pacific Ocean is likely to increase in the future warming climate, although the total number of tropical cyclones may decrease [Knutson *et al.*, 2010]. Previous studies also suggested that cyclones and typhoons can modify the partial pressure of CO_2 at the sea surface ($p\text{CO}_{2\text{sea}}$) [Bates *et al.*, 1998; Perrie *et al.*, 2004; Nemoto *et al.*, 2009; Huang and Imberger, 2010; Levy *et al.*, 2012]. More studies remain to be done, however, about the effects of extreme weather conditions (such as typhoons, hurricanes, tropical cyclones, and winter storms) on the $p\text{CO}_{2\text{sea}}$ and air-sea CO_2 flux under the presence of cyclonic (cold) or anticyclonic (warm) eddies [Hood *et al.*, 2001; Sun *et al.*, 2014].

The South China Sea (SCS) is one of the largest semienclosed marginal seas in the world. This region is frequently affected by tropical cyclones or typhoons. The total dissolved inorganic carbon (DIC), total alkalinity (TA), and $p\text{CO}_2$ in the SCS were found to increase with depth, which were, respectively, about $2200 \mu\text{mol kg}^{-1}$, $1890 \mu\text{mol kg}^{-1}$, and $370 \mu\text{atm}$ at the sea surface and about $2280 \mu\text{mol kg}^{-1}$, $2080 \mu\text{mol kg}^{-1}$, and $500 \mu\text{atm}$ below 150 m [Tseng *et al.*, 2007]. The annual values of $p\text{CO}_{2\text{sea}}$ in this region were found to be between 360 and 425 μatm , with seasonal changes found to vary between 8 and 40 μatm in autumn [Zhai *et al.*, 2005, 2013]. At the SEATS station (18°N , 116°E) close to our study region, the seasonal variation in $p\text{CO}_{2\text{sea}}$ ranged between 340 and 395 μatm [Tseng *et al.*, 2007]. In autumn, the mixed layer depth (MLD) at SEATS was found to be about 20 m, and $p\text{CO}_2$ was nearly constant in the upper 40 m and increases with depth below 40 m [Tseng *et al.*, 2007].

With a steady increase in the atmospheric CO₂ concentration, the ocean plays a more important role than ever in mitigating climate change [Le Quéré *et al.*, 2009]. The oceanic storage of the anthropogenic CO₂ is affected significantly by the air-sea flux of CO₂ at the sea surface. The latter depends on the difference between the partial pressure of CO₂ at the oceanic surface water (pCO_{2sea}) and atmosphere (pCO_{2air}), as well as the wind speed, sea surface temperature (SST), and sea surface salinity (SSS) [Wanninkhof, 1992; Wanninkhof *et al.*, 2009]. In comparison with the relatively stable distribution of pCO_{2air}, the spatial distribution of pCO_{2sea} is highly variable and plays a very important role in determining the temporal and spatial variability in the air-sea flux of CO₂ at the sea surface due to its sensitivity to episodic events. Distributions of pCO_{2sea} depend strongly on four important state variables including the SST, DIC, TA, and SSS [Takahashi *et al.*, 1993]. The pCO_{2sea} values are also affected by other physical, chemical, and biological processes in the ocean. Takahashi *et al.* [2002] estimated that the average biological drawdown of pCO_{2sea} in surface waters was about 35 μatm in the subtropical waters between 30°N and 30°S, and exceeded 140 μatm in high-latitude oceans to the north of about 40°N. The processes such as vertical mixing, tides, currents, solar radiation, rainfall, and many biological activities were also found to have a great impact on the pCO_{2sea} by influencing the above mentioned four state variables. Extreme storms such as typhoons (or hurricanes) were found to have a great impact on the marine ecosystem. The storm-induced processes reported in the literature include the intense SST cooling behind the storm [Price, 1981; Sheng *et al.*, 2006; Ko *et al.*, 2014; Huang and Oey, 2015], phytoplankton bloom both at the surface [Zhao *et al.*, 2009] and subsurface [Ye *et al.*, 2013], high export of particulate organic carbon out of the euphotic zone [Hung *et al.*, 2010; Shih *et al.*, 2013], and storm-induced increase in fish abundance [Yu *et al.*, 2014]. Typhoon-induced upper ocean mixture and entrainment of deep water and the storm-induced air-sea heat exchange can lead to the SST cooling [Price, 1981; Lin *et al.*, 2009; Ye *et al.*, 2013], which decreases pCO_{2sea} by about 4.23% per °C [Takahashi *et al.*, 1993]. On the other hand, the entrainment of higher DIC waters from the thermocline into the surface mixed layer increases the oceanic pCO_{2sea} [Wanninkhof *et al.*, 2007; Koch *et al.*, 2009; Sun *et al.*, 2014]. Biological metabolic processes, such as photosynthesis, respiration, and calcium carbonate precipitation or dissolution, can also alter the mass balance of the carbonate system and thus affect the pCO_{2sea} [Dai *et al.*, 2009; Krause-Jensen and Sand-Jensen, 1998]. A typhoon typically accompanies large precipitations. It was found that heavy rain can induce significant chemical dilution and reduce the pCO_{2sea} by more than 30 μatm in the low-wind and high-precipitation regions [Turk *et al.*, 2010; Sun *et al.*, 2014]. Furthermore, the presence of cyclonic eddies was found to either decrease or increase pCO_{2sea} [Chen *et al.*, 2007], while anticyclonic eddies were found to increase pCO_{2sea}.

Based on field observations and model results, several studies demonstrated that typhoons can cause enormous air-sea CO₂ flux (F_{CO₂}) from the ocean to the atmosphere (efflux) or vice versa (influx), which in turn affect the annual F_{CO₂} either locally [Bates *et al.*, 1998; Perrie *et al.*, 2004; Nemoto *et al.*, 2009; Sun *et al.*, 2014] or globally [Huang and Imberger, 2010]. Levy *et al.* [2012] found, in contrast, a very weak contribution from typhoons to global F_{CO₂} based on model results of 1663 historical typhoons. It is expected that the actual impact of a typhoon on F_{CO₂} depends on the oceanographic condition during the typhoon passage. Through the increased transfer velocity and indirectly by chemical dilution due to a large precipitation, heavy rain accompanied by a typhoon can decrease the air-sea pCO₂ in the ocean sink regions or turn a weak source to a sink in the ocean source regions [Turk *et al.*, 2010; Sun *et al.*, 2014]. Furthermore, thermal fronts act as a source or sink depends on the strength of the mixing process associating with biological response and phase of the front [Sarma *et al.*, 2015].

Impact of episodic events on the pCO_{2sea} and F_{CO₂} was reasonably studied in the past. Only a few studies, however, were made on the combined effects of a cyclonic or anticyclonic eddy and rainfall under the impact of a typhoon on the pCO_{2sea} and F_{CO₂}. The passage of a tropical depression was found to change the SCS from influx into efflux under the combined effect of rainfall and a preexisted cold eddy [Sun *et al.*, 2014]. The present study aims to investigate the important effects of a typhoon, rainfall, preexisted cold, and warm eddies on the pCO_{2sea} and local F_{CO₂} over the northern South China Sea (NSCS).

The paper is organized as follows. The data and methods used in this study are described in section 2. Analyses of in situ observations and satellite remote sensing data over the NSCS during Typhoon Wutip are presented in section 3. Discussion on spatial variability of pCO_{2sea} over the NSCS during Typhoon Wutip is given in section 4. A summary and conclusions are given in section 5.

2. Data and Methods

2.1. Satellite Products, Typhoon Data, and In Situ Data

2.1.1. Typhoon Data

Wutip was a Category 2 typhoon based on the Saffir-Simpson hurricane scale. Wutip originated from a tropical depression in the central South China Sea at 1800 UTC (Coordinated Universal Time) on 26 September 2013 (weather.unisys.com/). The storm moved northward and then westward on 27 September. Wutip strengthened to a typhoon at 0600 UTC on 28 September, with an average maximum sustained wind (MSW) of $\sim 117 \text{ km h}^{-1}$. The storm lingered over an area centered at (114.2°E, 16.5°N) for about 24 h (Figure 1). During its lingering period, Wutip became a Category 2 typhoon with the MSW of $\sim 126 \text{ km h}^{-1}$ and a slow translation speed of $\sim 0.54 \text{ m s}^{-1}$ (or $\sim 1.9 \text{ km h}^{-1}$). From 0000 UTC to 1200 UTC on 29 September, Typhoon Wutip reached its MSW of 163 km h^{-1} , with a fast translation speed of 3.9 m s^{-1} . Wutip made a landfall at 0600 UTC on 30 September.

The storm track data for Typhoon Wutip to be used in this study were taken from the Joint Typhoon Warning Center (weather.unisys.com/hurricane/). The storm track data set consists of 6 hourly time series of locations of the typhoon center and the maximum sustained wind speeds at 10 m above the mean sea level. The translation speeds of Wutip were estimated from time-varying positions of its center.

2.1.2. Satellite Products

Six different satellite data sets are used in this study to examine atmospheric and oceanographic conditions at the sea surface of the NSCS before, during, and after the passage of Typhoon Wutip. The daily multiscale ultrahigh resolution (MUR) SST analysis data with a horizontal resolution of $0.01^\circ \times 0.01^\circ$ were obtained from the website of the NASA Jet Propulsion Laboratory at data.nodc.noaa.gov/ghrsst/L4/GLOB/JPL/MUR/. The daily remote sensing fields of sea surface winds (at 10 m above the mean sea level) with a $0.25^\circ \times 0.25^\circ$ resolution were obtained from the Advanced Scatterometer (ASCAT) website at ftp.ifremer.fr/ifremer/cersat/products/gridded/MWF/L3/ASCAT/. The 3 h rainfall fields with the same horizontal resolution of $0.25^\circ \times 0.25^\circ$ were obtained from the website for the Tropical Rainfall Measuring Mission (TRMM) at disc2.nascom.nasa.gov/data/TRMM/. Daily fields of absolute geostrophic velocities at the sea surface derived from the

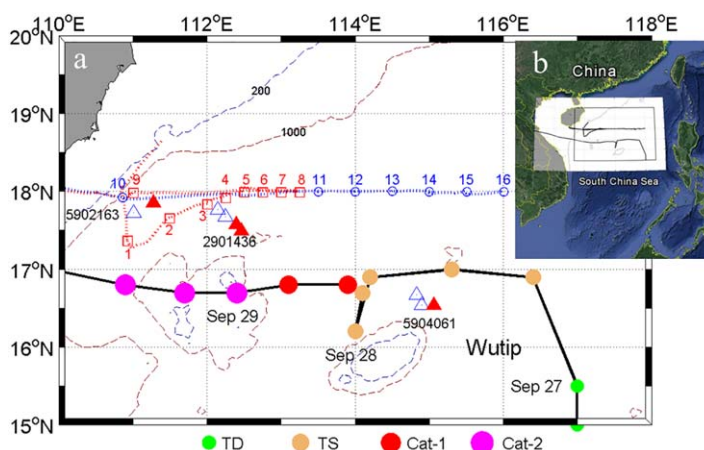


Figure 1. (a) The study region of the north South China Sea between 110°E and 118°E and between 15°N and 20°N; the storm track (black thick line) of Typhoon Wutip in September 2013; tracks of scientific cruises (red and blue dashed lines); stations of in situ oceanographic measurements (squares and circles with numbers); and positions of three Argo floats (triangles). Red squares and blue circles represent cruise stations conducted on 25–27 September (before the passage of Typhoon Wutip) and on 1–2 October (after the passage of Typhoon Wutip). The 6 h positions of typhoon centers are marked by colored dots along the storm track, of which sizes and colors represent the typhoon intensity. Red and blue dashed lines represent cruise tracks before and after the passage of Typhoon Wutip. Solid red triangles and open blue triangles represent Argo float stations before and after the typhoon’s passage. Blue and brown dashed lines represent 200 and 1000 m water depths, respectively. Abbreviations are used for tropical depression (TD), tropical storm (TS), category-one typhoon (Cat-1), and category-two typhoon (Cat-2). (b) Google map showing the study region, storm track of Typhoon Wutip, and cruise tracks within the South China Sea.

merged altimeter products and merged sea level anomaly (SLA) were obtained from the website for the Archiving, Validation and Interpretation of Satellite Oceanographic data (AVSIO) at www.aviso.oceanobs.com.

The sea surface phytoplankton chlorophyll a concentration (Chla) product with a spatial resolution of 1 km derived from the daily Visible Infrared Imaging Radiometer Suite (VIIRS) was obtained from the website of the NASA OceanColor at oceancolor.gsfc.nasa.gov/cms/data/viirs. The daily surface heat flux fields with a $0.5^\circ \times 0.5^\circ$ resolution were extracted from the National Centers for Environmental Prediction climate forecast system version 2 (rda.ucar.edu/datasets/).

2.1.3. In Situ Observations

A field program organized by the South China Sea Institute of Oceanography, Chinese Academy of Science was conducted

on 25–27 September and 1–2 October 2013 (Figure 1). During this field program, the SST and SSS were measured and recorded every 5 s with a SEACAT CTD (SBE21, Sea-Bird Co.) along the cruise tracks marked in Figure 1. Except for segments of the first cruise track moving southward from a position near Station 10 to Station 1 then from Station 1 to Station 3, most of the cruise tracks were parallel to a zonal transect at 18°N, which is about 110 km to the north of the storm track of Typhoon Wutip. Along these cruise tracks, $pCO_{2\text{sea}}$ and $pCO_{2\text{air}}$ were measured alternatively by the automated flowing pCO_2 measuring system (GO8050, General Oceans, Inc., USA) [Sun *et al.*, 2014]. To eliminate the influence of coastal waters on $pCO_{2\text{sea}}$, all the $pCO_{2\text{sea}}$ data collected at depths less than 200 m were excluded in this study (Figure 1). The observed pCO_2 data were quality-controlled according to the World Ocean Circulation Experiment guidelines [Pierrot *et al.*, 2009]. First, all in situ measurements made with the ship speeds of less than 5 m s^{-1} were eliminated. Second, within one measurement period, each $pCO_{2\text{sea}}$ or $pCO_{2\text{air}}$ greater than one standard deviation was not considered and replaced by the mean value during the measurement period. One measurement period in this study is referred to as a duration during which the $pCO_{2\text{air}}$ was measured 10 times and then the $pCO_{2\text{sea}}$ was measured 20 times.

Vertical profiles of temperature and salinity at 16 stations along the cruise tracks were measured by a CTD (Conductivity-Temperature-Depth) probe (Figure 1) during the field program. At all CTD stations except for Stations 4 and 16, Chla was determined by fluorescence based on the methodology suggested by Ye *et al.* [2013]. The hydrographic profiles of three Argo floats to be used in this study were extracted from the International Argo Program (www.argodatamgt.org/).

2.2. Methodology of Data Analysis

2.2.1. Mixed-Layer Depth and Ekman Pumping Velocity

The surface mixed-layer depth (MLD) to be used in this study is defined as the depth at which the temperature is 0.5°C lower than the mean value in the upper 10 m of the water column [Monterey and Levitus, 1997]. The Ekman pumping velocity (EPV) is calculated from the surface wind stress vector ($\vec{\tau}$) based on,

$$EPV = -\text{Curl}_z \left(\frac{\vec{\tau}}{\rho_a f} \right), \quad (1)$$

with

$$\vec{\tau} = \rho_a C_d |\vec{U}_{10}| \vec{U}_{10}, \quad (2)$$

where ρ_o is the seawater density set to 1025.0 kg m^{-3} , ρ_a is the air density set to 1.25 kg m^{-3} , f is the Coriolis parameter, $C_d = (2.229 + 0.02983U_{10} - 0.00468U_{10}^2)$ is the drag coefficient [Jarosz *et al.*, 2007], and \vec{U}_{10} is the wind velocity vector at 10 m above the mean sea level.

2.2.2. Air-Sea CO_2 Flux

The CO_2 flux across the air-sea interface (noted as F_{CO_2}) is often estimated from the bulk formula given as:

$$F_{CO_2} = k \times K_H \times (pCO_{2\text{sea}} - pCO_{2\text{air}}), \quad (3)$$

where k is the gas transfer velocity of CO_2 , K_H is the solubility of CO_2 in seawater [Weiss, 1974], and $pCO_{2\text{sea}}$ and $pCO_{2\text{air}}$ are the partial pressure of CO_2 in water and air, respectively. A positive value of F_{CO_2} represents the net CO_2 flux from sea to atmosphere (efflux) and a negative value represents the net CO_2 exchange from atmosphere to sea (influx). Since the gas transfer velocity (k) was not measured over the study region, we follow Wanninkhof [1992] and calculate it based on,

$$k = 0.31 \left(|\vec{U}_{10}| \right)^2 (S_c / 660)^{-0.5}, \quad (4)$$

where S_c is the Schmidt number for CO_2 in the seawater, 660 is the value of S_c at $S = 35$ (psu) and $T = 20^\circ\text{C}$, and 0.31 is a proportionality factor. Wanninkhof [1992] suggested that equation (4) is applicable for estimating gas transfer velocities at steady winds, from spot measurements using shipboard anemometers, and from wind speeds derived from scatterometers or radiometers. In equation (4) the gas transfer velocity (k) takes the units of cm h^{-1} , and the wind speed $|\vec{U}_{10}|$ takes units of m s^{-1} . The equation suggested by Wanninkhof [1992] can be used to compute S_c ,

$$S_c = 2073.1 - 125.62 \times SST + 3.6276 \times SST^2 - 0.043219 \times SST^3. \quad (5)$$

The solubility of CO_2 ($\text{mol L}^{-1} \text{atm}^{-1}$) in the seawater can be expressed as [Weiss, 1974],

$$\begin{aligned} \ln K_H = & -58.0931 + 90.5069 \times \left(\frac{100}{\theta}\right) + 22.294 \times \ln\left(\frac{\theta}{100}\right) \\ & + S \times \left[0.027766 - 0.025888 \times \left(\frac{\theta}{100}\right) + 0.0050578 \times \left(\frac{\theta}{100}\right)^2 \right], \end{aligned} \quad (6)$$

where θ is the absolute water temperature and S is the salinity in psu.

3. Results

3.1. In Situ Observations of SST, SSS, and pCO_2

Figure 2 presents distributions of SST, SSS, $\text{pCO}_{2\text{sea}}$, and F_{CO_2} before and after Typhoon Wutip along a zonal transect between 110°E and 116°E at $\sim 18^\circ\text{N}$. This zonal transect was roughly parallel to the storm track of Typhoon Wutip and located at about 110 km to the right of the storm track (when facing in the direction taken by the storm). On 25–27 September (before the typhoon), the observed SST at the zonal transect (red symbols in Figure 2a) was nearly uniform zonally, with the averaged SST of about $29.06 \pm 0.25^\circ\text{C}$ (the second number is one standard deviation). During this pretyphoon period, there were relatively low SSTs of less than 28.9°C between 111.4°E and 112.4°E , and relatively high SSTs of greater than 29.4°C between 113.2°E and 113.25°E (Figure 2a). On 1–2 October (after the typhoon), by comparison, the observed SSTs at the zonal transect (blue symbols in Figure 2a) had significant spatial variations, with the averaged SST of about $27.87 \pm 1.07^\circ\text{C}$. During this posttyphoon period, low surface waters of less than 28°C occurred between 110.8°E and 113.2°E , with the lowest SST of about 26°C centered at 112.0°E along the zonal transect. As will be discussed later, these low SST waters were generated mostly by Typhoon Wutip. During this posttyphoon period, high SST waters of greater than 28.6°C were observed between 113.2°E and 116.0°E along the transect.

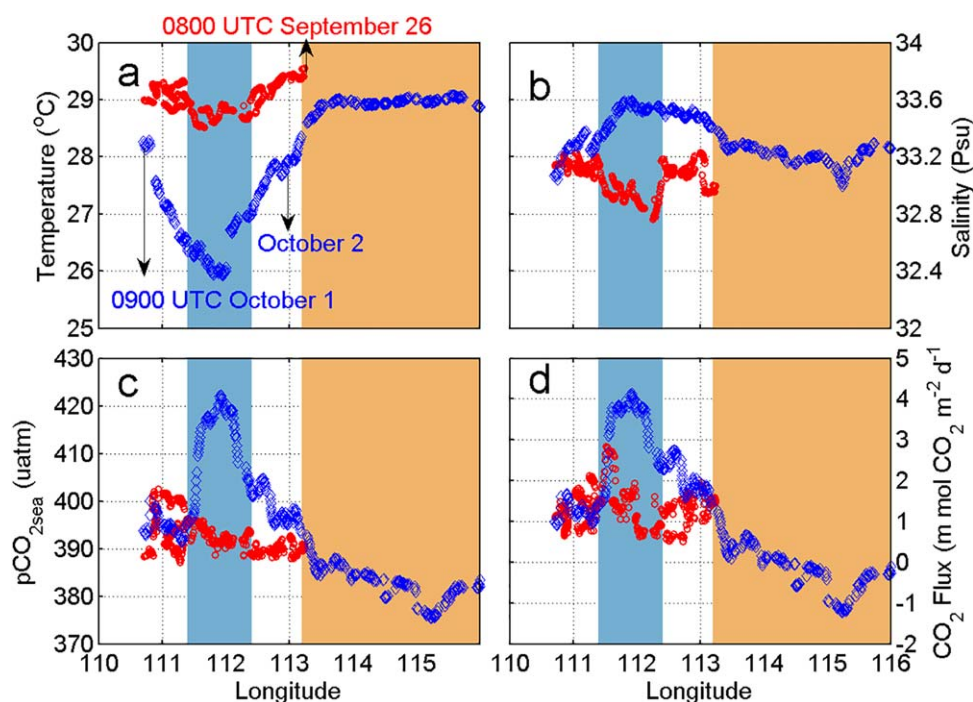


Figure 2. Longitudinal distributions of in situ measurements of (a) sea surface temperature, (b) sea surface salinity, (c) $\text{pCO}_{2\text{sea}}$, and (d) air-sea CO_2 flux along the cruise tracks near 18°N . The red and blue symbols represent in situ measurements on 25–27 September and 1–2 October, respectively. Areas marked by royal blue and orange colors represent the small-size cyclonic eddy water mass (CEIN) and large-size anticyclonic eddy water mass (AEIN) during the study period, respectively. Black arrows mark times of in situ measurements conducted.

Table 1. Area-Averaged Pretyphoon and Posttyphoon Values of the Sea Surface Temperature (SST), Sea Surface Salinity (SSS), Mixed-Layer Depth (MLD), Partial Pressure of CO₂ at the Sea Surface (pCO_{2sea}), and Air-Sea CO₂ Flux (F_{CO2}) Over Three Different Water Masses Along Cruise Tracks at ~18°N^a

Water Masses	Location (°E)	Sample Size	SST (°C)	MLD (m)	SSS (psu)	pCO _{2sea} (μatm)	F _{CO2} (mmol CO ₂ m ⁻² d ⁻¹)
Before the Passage of Typhoon Wutip							
CEIN	111.4–112.4	111	28.75 ± 0.12	23	32.94 ± 0.08	392.92 ± 1.83	1.44 ± 0.61
OUT	110.7–111.4	275	29.16 ± 0.17	32	33.12 ± 0.06	393.04 ± 4.31	1.24 ± 0.38
	112.4–113.2						
AEIN	113.2–113.25	12	29.50 ± 0.07	51	32.98 ± 0.02	390.31 ± 0.50	1.51 ± 0.05
Mean			29.06 ± 0.25		33.07 ± 0.11	392.93 ± 3.74	1.31 ± 0.46
After the Passage of Typhoon Wutip							
CEIN	111.4–112.4	93	26.39 ± 0.37	14	33.52 ± 0.07	413.05 ± 7.56	3.30 ± 0.75
OUT	110.7–111.4	148	27.51 ± 0.52	39	33.40 ± 0.13	396.97 ± 3.42	1.71 ± 0.51
	112.4–113.2						
AEIN	113.2–116	181	28.94 ± 0.10	49	33.22 ± 0.07	383.03 ± 3.72	-0.11 ± 0.55
Mean			27.87 ± 1.07		33.35 ± 0.15	394.53 ± 12.54	1.28 ± 1.46

^aThese three different water masses are (a) large-size anticyclonic eddy water (AEIN) over the central region of the north South China Sea, (b) small-size cyclonic eddy water (CEIN) to the west of the AEIN, and (c) water mass surrounding the AEIN (OUT).

The pretyphoon SSS was also observed to have noticeable spatial variability along the zonal transect with low SSS of less than 33 (psu) between 111.7°E and 112.4°E and between 113.10°E and 113.25°E (red symbols in Figure 2b). The averaged pretyphoon SSS at the transect was about 33.07 ± 0.11. After the typhoon, the observed SSS had significant zonal variability (blue symbols in Figure 2b), with high SSS greater than 33.4 over 111.53°E–113.18°E and low SSS of less than 33 centered at about 115.25°E. The averaged SSS after the typhoon was about 33.35 ± 0.15. It should be noted that the observed SSS between 111.7°E and 112.4°E at the zonal transect was significantly increased by Typhoon Wutip (Figure 2b).

The averaged pCO_{2sea} was about 392.93 ± 3.74 μatm with some noticeable spatial variations on 25–27 September before the typhoon (red symbols in Figure 2c). By comparison, very large spatial variations in pCO_{2sea} occurred after the typhoon, with the averaged value of about 394.53 ± 12.54 μatm on 1–2 October after the typhoon (blue symbols in Figure 2c). Due to the impact of the typhoon, the maximum value of pCO_{2sea} had an increase of about 30 μatm from about 391.42 μatm at about (111.93°E, 17.98°N) before the typhoon to about 422.20 μatm at about (111.93°E, 17.95°N) after the typhoon (Figure 2c). The posttyphoon sea surface water with the lowest pCO_{2sea} value of about 375.70 μatm occurred at about (115.25°E, 17.98°N) along the zonal transect.

The offshore surface waters along the zonal transect were oversaturated with the averaged F_{CO2} value of about 1.31 ± 0.46 mmol CO₂ m⁻² d⁻¹ on 25–27 September before the typhoon (red symbols in Figure 2d). On 1 and 2 October after the typhoon, the averaged F_{CO2} value was about 1.28 ± 1.46 mmol CO₂ m⁻² d⁻¹ (blue symbols in Figure 2d). Due to the effect of the typhoon, the maximum value of F_{CO2} raised to about 4.12 mmol CO₂ m⁻² d⁻¹ at about (111.93°E, 17.95°N) from ~1.0 mmol CO₂ m⁻² d⁻¹ before the typhoon. After the typhoon, the minimum value of F_{CO2} dropped to about -1.22 mmol CO₂ m⁻² d⁻¹ at about (115.20°E, 17.98°N) (Table 1).

The SST-pCO_{2sea} and SSS-pCO_{2sea} diagrams are used to examine the dependence of pCO_{2sea} and F_{CO2} on the SST and SSS. Before the typhoon on 25–27 September, pCO_{2sea} was not strongly correlated with SST and SSS (Figures 3a and 3b). After the typhoon on 1–2 October, by contrast, pCO_{2sea} was strongly correlated with SST and SSS, respectively (R² = 0.79, p < 0.001 and R² = 0.73, p < 0.001) (Figures 3c and 3d). The results shown in Figure 3 indicate that physical processes played a much more important role in affecting pCO_{2sea} after the typhoon than before the typhoon. More discussion about this point will be given later.

3.2. Wind and EPV Affected by Typhoon Wutip

As mentioned earlier, Wutip originated from a tropical depression in the central South China Sea on 26 September 2013. This storm moved into the study region on 27 September and left the study region near the end of 29 September (Figure 1). During this 3 day period, Wutip reached a typhoon status at 0600 UTC on 28 September and became a Category 2 typhoon with the mean MSW of about 160 km h⁻¹ (or about 44 m s⁻¹) on 29 September. Figure 4a (row A) presents the 3 day time-mean wind speeds and directions averaged from the daily ASCAT image data before the typhoon on 24–26 September. The pretyphoon

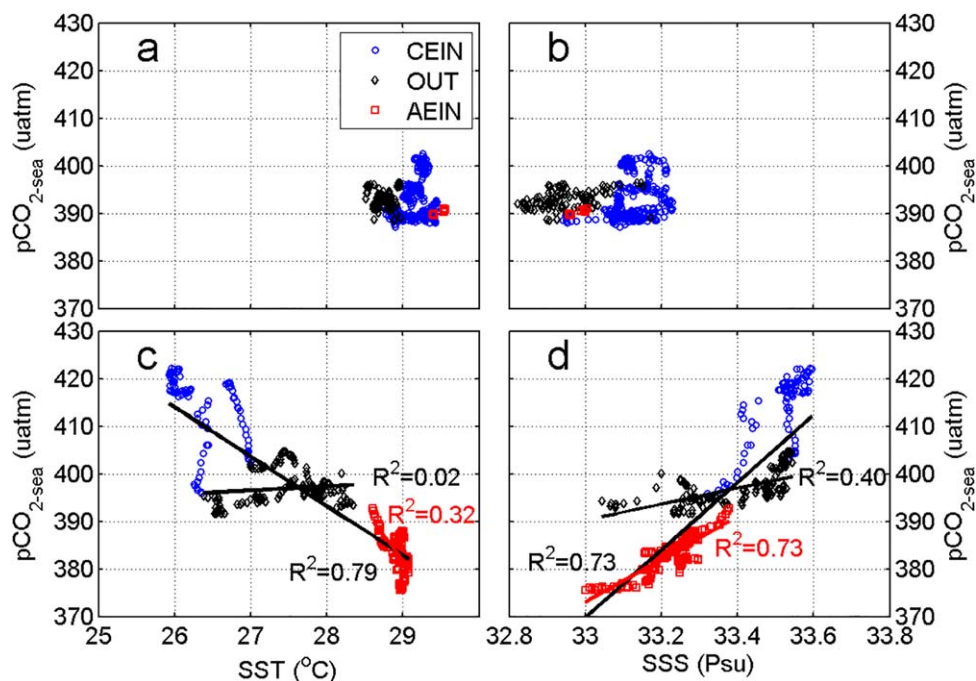


Figure 3. Scatterplots between different in situ measured oceanographic variables measured at the sea surface: (a) SST versus $p\text{CO}_{2\text{sea}}$ and (b) SSS versus $p\text{CO}_{2\text{sea}}$ before the typhoon on 25–27 September, and (c) SST versus $p\text{CO}_{2\text{sea}}$ and (d) SSS versus $p\text{CO}_{2\text{sea}}$ after the typhoon on 1–2 October. Blue circles, black diamonds, and red squares correspond to in situ measurement in the cyclonic eddy water (CEIN), surrounding water (OUT), and the anticyclonic eddy water (AEIN), respectively.

time-mean winds over the study region are characterized by relatively weaker winds of less than 5 m s^{-1} over the southwestern part, and relatively stronger winds of about 9 m s^{-1} over the northeastern part of the study region. The westward and southwestward winds prevailed over the northern part of the study region during this period.

During the typhoon on 27–29 September, strong winds with a large-scale cyclonic pattern prevailed over the whole study region, with very strong winds of greater than 15 m s^{-1} over the northwestern part of the study region and weaker winds over other areas (Figure 4b, row A). During this period, the 3 day time-mean winds were strong and about 16.8 m s^{-1} over the Wutip's lingering area centered at about (114.1°E , 16.5°N). Along the zonal transect at 18°N , the mean wind speed during Typhoon Wutip was about 11.7 m s^{-1} and only 2–3 times higher than the winds before the typhoon, which is expected since this zonal transect is about 110 km away from the storm track. It should be noted that the horizontal structure of surface winds inside the typhoon was not resolved well by the ASCAT remote sensing data set (Figure 4b, row A), due mainly to its relatively coarse horizontal resolution of 26 km in comparison with the typical radius (about 150 km) of Typhoon Wutip.

The 3 day time-mean winds weakened significantly and were nearly westward after the typhoon between 30 September and 2 October (Figure 4c, row A), with the time mean winds of less than 5 m s^{-1} over the southeastern part and about 7 m s^{-1} over the northern part of the study region. The posttyphoon time-mean wind speed was about 7.5 m s^{-1} along the zonal transect at 18°N , which was much weaker than the time-mean wind during the typhoon, but highly comparable to the time-mean wind before the typhoon (Figure 4a, row A).

Distributions of Ekman pumping velocities (EPVs) indicate that the wind-induced upwelling before the typhoon (24–26 September; Figure 4a, row B) was very weak over the most of the study region, except for small values ($< 2.5 \times 10^{-5} \text{ m s}^{-1}$) over the southeastern part of the region. During the passage of Typhoon Wutip on 27–29 September, the large and positive EPVs (greater than $5 \times 10^{-5} \text{ m s}^{-1}$) occurred along the storm track and areas to the right of the storm track (Figure 4b, row B), with the largest EPV of about $3.3 \times 10^{-4} \text{ m s}^{-1}$ over the lingering area of Typhoon Wutip. These large and positive EPVs indicate occurrence of strong wind-induced upwelling during this period. It should be noted that over several small areas to the

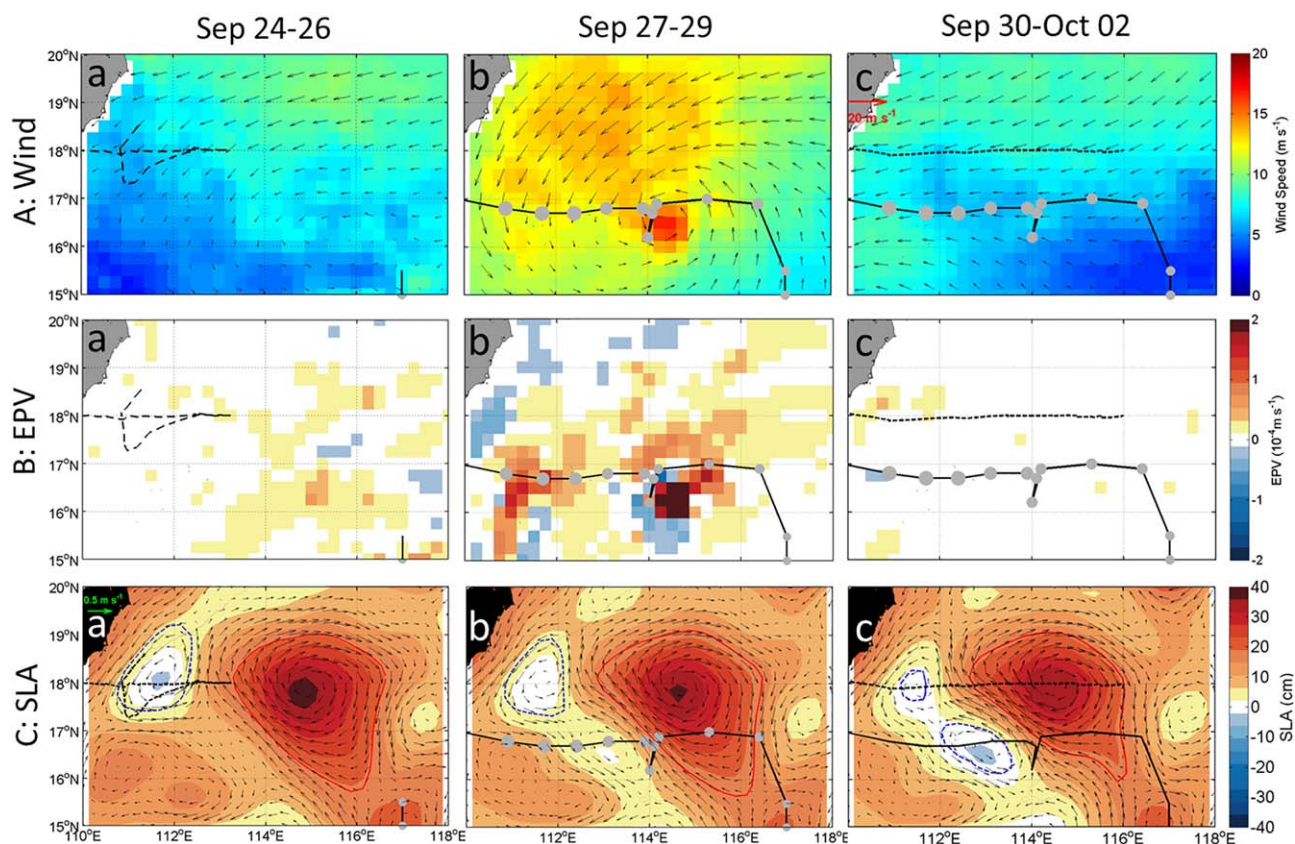


Figure 4. Satellite remote sensing data of (a) surface wind speeds (m s^{-1}) and directions (arrows), (b) Ekman pumping velocity (EPV, m s^{-1}), and (c) sea level anomalies (SLA, cm) and absolute geostrophic currents at the sea surface (m s^{-1}) over the northern South China Sea. Left, middle, and right figures are satellite data before, during, and after the passage of Typhoon Wutip. Dashed lines represent cruise tracks. Black solid lines and gray dots represent the storm track and intensity of Typhoon Wutip.

left of the storm track, there were large and negative EPVs, indicating also the occurrence of wind-induced downwelling over these small areas (Figure 4b, row B). Along the zonal transect at 18°N over the lingering area, the mean EPVs during Typhoon Wutip was about $2.8 \times 10^{-5} \text{ m s}^{-1}$, which was 3 times larger than the pretyphoon value. The posttyphoon EPVs were weakened to about $0.3 \times 10^{-5} \text{ m s}^{-1}$ over the most of the study region (Figure 4c, row B).

3.3. Geostrophic Circulation and Eddy Fields

In addition to typhoon-induced currents, upwelling/downwelling and vertical mixing during Typhoon Wutip, distributions of pCO_2 were also affected by the large-scale oceanic circulation over the NSCS. Here we focus on the absolute geostrophic currents at the sea surface derived from the satellite altimeter data and merged SLA fields. Figure 4a (row C) demonstrates that before the typhoon on 24–26 September, a large-size anticyclonic eddy occurred over the central part of the NSCS, with its center located at about (115°E , 18°N) and the maximum speed of about 0.53 m s^{-1} . To the west of this large-size anticyclonic eddy, a small-size cyclonic eddy occurred with its center located at about (111.75°E , 18.25°N) and the maximum speed of about 0.35 m s^{-1} during this pretyphoon period (Figure 4a, row C). Furthermore, there were two weaker and less well-defined cyclonic eddies over the southwest part of the NSCS and one smaller-size cyclonic eddy to the east of the large-size anticyclonic eddies. Figure 4a (row C) also demonstrates that the in situ observations were made only over the cyclonic eddy and its adjacent waters during the pretyphoon period.

During the passage of Typhoon Wutip on 27–29 September, the large-size anticyclonic eddy reduced its size and moved gradually westward with its center relocated at (114.75°E , 18°N) (Figure 4b, row C). To the west of this anticyclonic eddy, the small-size cyclonic eddy reduced significantly its size and strength during this period. Some waters leaked out from this cyclonic eddy to develop a new cyclonic eddy to the southwest of the center of the large-size anticyclonic eddy (Figure 4b, row C). It should be noted that there were

no in situ observations made over the NSCS during this period due to the severe and dangerous marine conditions generated by Typhoon Wutip.

The large-size anticyclonic eddy moved further westward with its size reduced significantly after the typhoon from 30 September to 2 October (Figure 4c, row C). The maximum surface geostrophic currents inside this anticyclonic eddy actually increased during this period due to enhanced horizontal gradients of the surface elevations inside the eddy. The cyclonic eddy to the west of the large-size anticyclonic eddy weakened significantly, while the newly generated cyclonic eddy to the southwest of the large-size anticyclonic eddy strengthened significantly during this posttyphoon period (Figure 4c, row C). During this posttyphoon period, in situ observations were made along the zonal transect at $\sim 18^\circ\text{N}$, which crossed the small-size cyclonic eddy, the large-scale anticyclonic eddy, and their adjacent waters.

For simplicity of discussions, the observed water mass along the cruise track between 111.4°E and 112.4°E inside the small-size cyclonic eddy is referred to as the cyclonic eddy water mass (CEIN). The observed water mass along the cruise track between 113.2°E and 116.0°E inside the large-size anticyclonic eddy is referred to as the anticyclonic eddy water mass (AEIN). The observed water mass surrounding the CEIN is referred to as OUT (Figure 2 and Table 1).

3.4. Satellite-Derived Rainfall, SST, and Net Heat Flux

In addition to storm-induced severe winds, Typhoon Wutip also brought a significantly large amount of rainfall. Before the typhoon on 24–26 September, the 3 day time-mean rainfall was generally low and less than 30 mm d^{-1} over most of the NSCS, with slightly large rainfall of great than 50 mm d^{-1} ahead of the storm over the southeastern part of the study region (Figure 5a, row A). During the passage of Typhoon Wutip on 27–29 September, the 3 day time-mean rainfall along the storm path increased up to 100 mm d^{-1} or greater (Figure 5b, row A), which was about 4 times of the pretyphoon rainfall on 24–26 September. Figure 5b (row A) also shows that the heaviest rainfall was mainly left biased during Typhoon Wutip, which

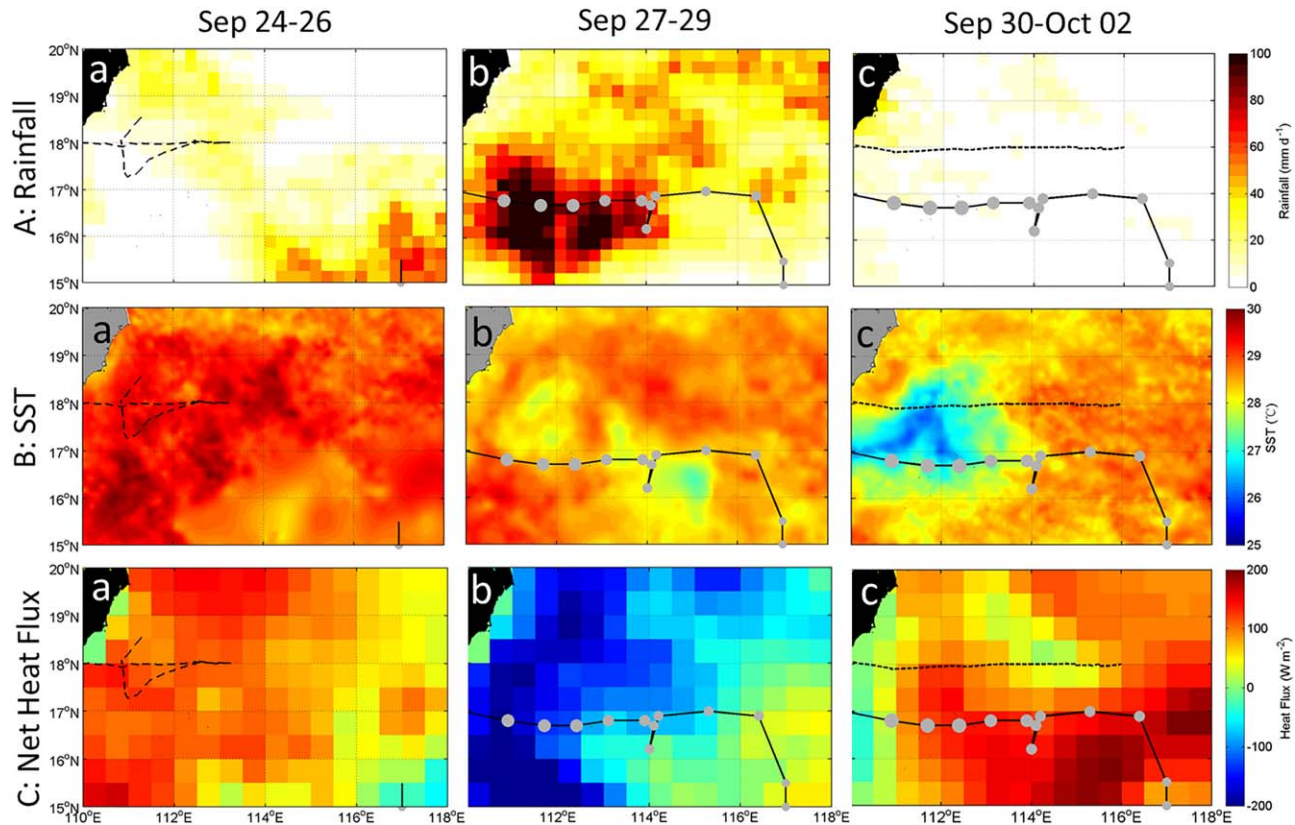


Figure 5. Satellite remote sensing data of (a) precipitation (shade, mm d^{-1}), (b) sea surface temperature (SST, $^\circ\text{C}$), and (c) heat flux (W m^{-2}). Left, middle, and right figures are satellite data before, during, and after the passage of Typhoon Wutip. Dashed lines represent cruise tracks. Black solid lines and gray dots represent the storm track and intensity of Typhoon Wutip.

differs from the typical rainfall distribution for a tropical cyclone [Lonfat *et al.*, 2004]. Usually, a larger proportion of rainfall falls in advance of the storm center than after the center's passage, with the highest percentage falling in the right front quadrant [Lonfat *et al.*, 2004], due to environmental factors such as wind shear, sea surface temperature, and moisture distribution. The rainfall was small after the typhoon from 30 September and 2 October (Figure 5c, row A).

Distributions of the 3 day time-mean SST on 24–26 September (Figure 5a, row B) are characterized by high SST of about 29°C in the study region before Typhoon Wutip. The pretyphoon SST was slightly warmer over the southwestern part and relatively cooler over the northern and southern part of the region. During the passage of Typhoon Wutip, there was significant SST cooling over areas under the direct effect of the storm. Except for the lingering area of the typhoon, the SST cooling was biased mainly to the right side of the storm track, which is consistent with previous findings [Price, 1981; Sheng *et al.*, 2006]. Over the lingering area of the typhoon, significant SST cooling of about 1.4°C occurred over a large area centered at about (115°E, 16.4°N) due mainly to the combined effect of storm-induced intense vertical mixing and strong upwelling. After the typhoon on 30 September to 2 October, significant SST cooling of about 3–4°C occurred over the area occupied by the small-size cyclonic eddy to the right of the storm track (Figure 5c, row B).

Distributions of the net heat flux at the sea surface shown in Figure 5 (row C) indicate that the net heat flux distributions had significant temporal and spatial variability before, during, and after the typhoon over the study region. Before the typhoon on 24–26 September, the 3 day time-mean net heat flux at the sea surface was positive and about 100 W m⁻² over the western part, and less than 40 W m⁻² over the eastern part of the study region (Figure 5a, row C). The net heat flux was negative over the southeast corner of the study region and near zero over coastal waters off southeastern Hainan Island during the pretyphoon period. During the passage of Typhoon Wutip, the net heat flux at the sea surface was large and negative of about -200 W m⁻² over the western part of the study region and moderate and positive of about 30 W m⁻² over the southeastern part of the study region (Figure 5b, row C). After the typhoon on 30 September to 2 October, the net heat flux at the sea surface was highly variable with positive values over areas to the left of the storm track, and slightly negative over the central area of the anticyclonic eddy and western part of the study region (Figure 5c, row C).

3.5. In Situ Observations of Temperature, Salinity, and Chlorophyll a

Discussions so far have been focused mostly on oceanographic conditions at the sea surface over the NSCS before, during and after Typhoon Wutip. A natural question to be asked is what was the response of subsurface hydrography to Typhoon Wutip. We address this issue by examining vertical profiles of observed hydrography. Figure 6 presents vertical profiles of temperature and salinity constructed from in situ observations at 14 CTD stations and 1 Argo float before the typhoon (measurements made between 110.7°E and 113.25°E) and after the typhoon (measurements made between 113.25°E and 115.0°E). During the pretyphoon period, the water mass with the relatively low temperature (<28.8°C) occurred at CTD Stations 3 and 4 and water mass with the relatively high temperature (>29°C) occurred at Stations 7 and 8 in the upper layer (Figure 6a). The combination of low temperature in the upper layer and shallow MLD centered at about (112°E, 18°N) is an indication of the occurrence of relatively strong upwelling at Station 3. Figure 6b indicates that a low-salinity patch (<33 psu) occurred at Stations 3 and 4 and another low-salinity patch occurred at Station 8, due mostly to the rainfall distribution during this sampling period (Figure 5a, row A). Due to the impact of Typhoon Wutip, water mass with relatively low temperature (<28.9°C) and high salinity (>33.2 psu) occurred at CTD Stations 11–15 in the upper layer, even although heavy rainfalls occurred during the passage of the storm (Figure 6).

In the surrounding water mass (OUT) to the west of the cyclonic eddy, in which Stations 9 and 10 were located, the MLD was about 33 m before the typhoon and increased to 44 m after the typhoon (Figures 6a and 7a). It should be noted that at depths about 15 m of Station 9 on 27 September, the observed salinity was very low and about 32.5 (Figure 7a). Exact reasons for these low-salinity subsurface waters are not known.

During the study period, Argo float 5902163 was located in the same surrounding water mass, but to the south of Stations 9 and 10 (Figure 1a). The MLD at this Argo float increased from 26 m before the typhoon to 34 m after the typhoon (Figures 6a and 7b). The decreased temperature and increased salinity in the

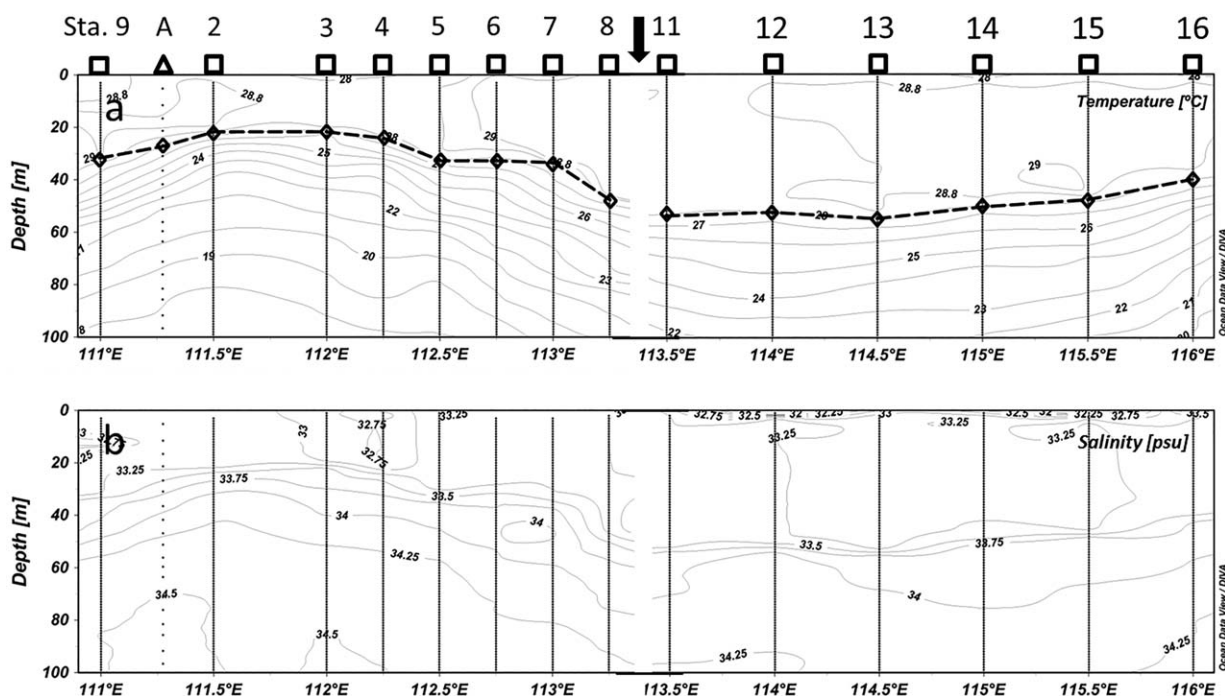


Figure 6. Vertical profiles of (a) temperature and (b) salinity along cruise tracks at $\sim 18^\circ\text{N}$. Black open squares represent CTD stations and the black open triangle represents Argo float 5902163 on 26 September. Dashed line and diamonds represent the mixed-layer depth. It should be noted that time-depth distributions of temperature and salinity between 110.7°E and 113.25°E were constructed from the observations made at Stations 9, A, and 2–8 before Typhoon Wutip. The time-depth distributions between 113.25°E and 116.0°E were constructed from observations made at Stations 11–16 after Wutip. The solid arrow represents the duration when Typhoon Wutip swept the southern part of the study region.

upper 30 m and increased temperature and decreased salinity at depths between 30 and 50 m indicated very strong vertical mixing caused by Typhoon Wutip. By comparison, relative small changes in temperature and salinity occurred at depths between 50 and 80 m and almost no change at depths greater than 80 m. This indicates that the observed temperature and salinity at depths greater than 80 m in this surrounding water mass were not affected by Typhoon Wutip (Figures 7a and 7b).

Argo float 2901436 was located inside the cyclonic eddy water mass (CEIN) during this study period (Figure 1a). Vertical profiles observed by this Argo float (Figure 7c) indicate that the MLD for the CEIN was about 32 m before the typhoon and decreased to 14 m on 1 October after the typhoon. The observed temperature and salinity at this Argo float were vertically more uniform on 27 and 29 September during the typhoon than the pretyphoon and posttyphoon conditions within the surface mixed layer. All of these indicate two important processes: (a) strong vertical mixing during the typhoon and (b) upwelling occurrence over this area as demonstrated by Figure 4b (row B). Figure 7c also demonstrates that the CEIN had significant changes in hydrographic (particularly temperature) profiles at depths between 40 and 200 m, which indicates the occurrence of strong upwelling induced by Typhoon Wutip up to 200 m.

It should be noted that at Argo float 2901436, the observed temperature (salinity) decreased (increased) at depths between 10 and 38 m, and increased (decreased) at depths between 38 and 85 m from 29 September to 1 October (Figure 7c). These large temporal changes in hydrography were associated mainly with intense vertical mixing generated by Typhoon Wutip. At depths greater than 100 m at this Argo float, the observed temperature slightly increased (and salinity was nearly uniform) during this 3 day period after the typhoon. Exact reasons for these temporal changes at depths greater 100 m are not known.

Vertical stratifications in the anticyclonic eddy water mass (AEIN) were also affected by Typhoon Wutip as demonstrated by the hydrographic observations made at Stations 8 and 11 (Figure 7d). These two stations were chosen since the CTD measurements were made at Station 8 before the typhoon and Station 11 after the typhoon and also since these two stations were close to each other. Furthermore, Station 8 was at the edge of the AEIN, and Station 11 was close to the center of the AEIN. Figure 7d demonstrated that nearly uniform temperature and salinity occurred in the top 50 m of the AEIN, due mainly to strong vertical mixing

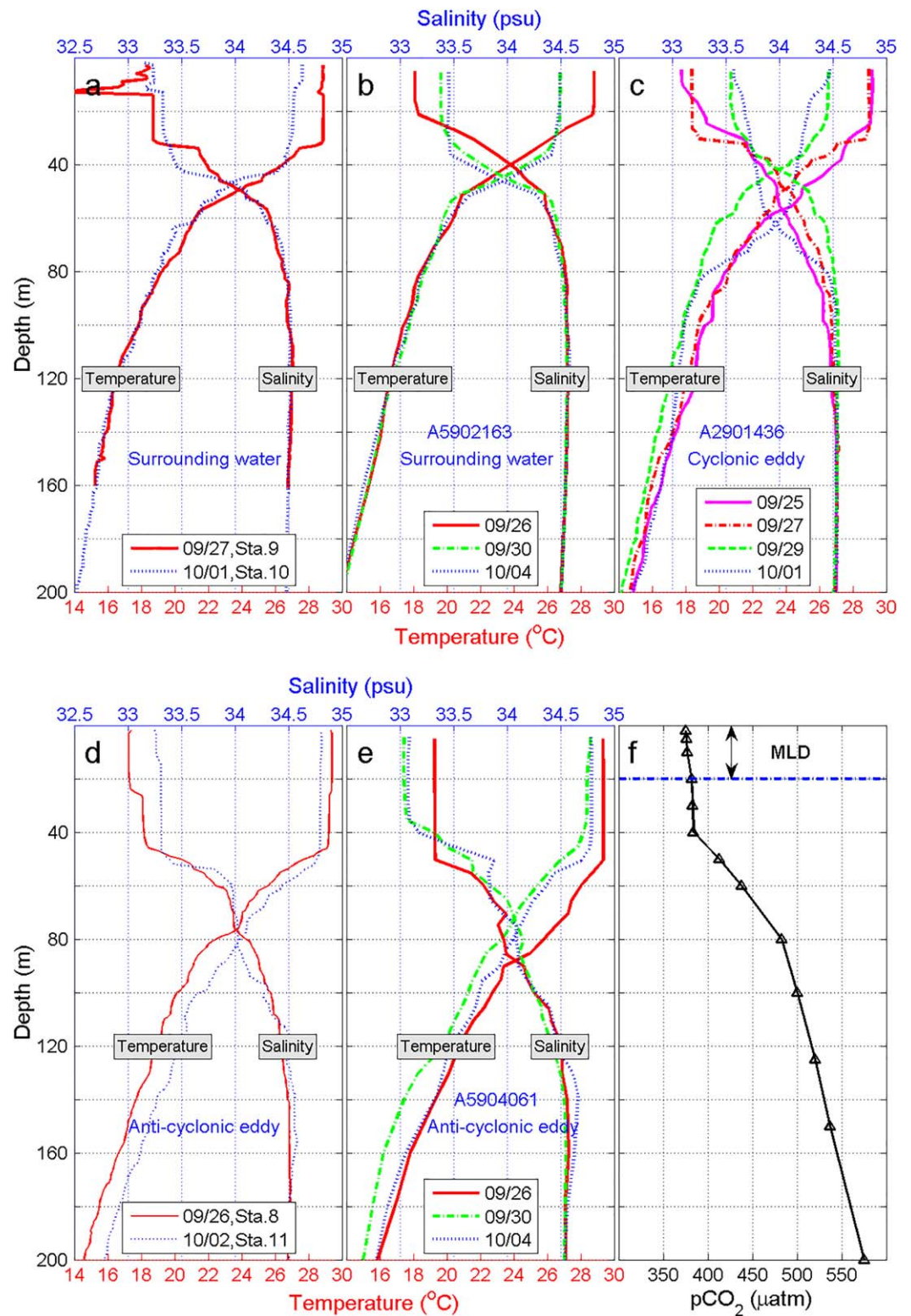


Figure 7. Vertical profiles of observed temperature and salinity in different water masses before and after the passage of Typhoon Wutip at (a) CTD Stations 9 and 10, (b) Argo float 5902163, (c) Argo float 2901436, (d) CTD Stations 8 and 11, and (e) Argo float 5904061. (f) Vertical profile pCO₂ from Tseng et al. [2007, Figure 4e].

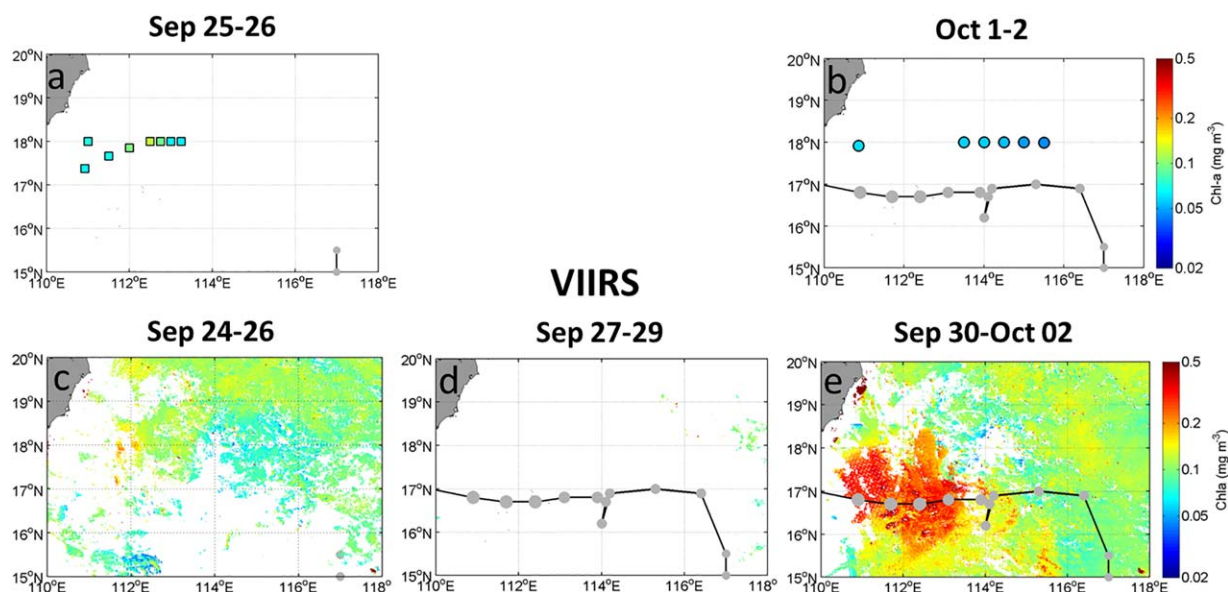


Figure 8. Distributions of chlorophyll a (Chla) at the sea surface derived from ship measurements (a) before the typhoon on 25–26 September and (b) after the typhoon on 1–2 October. Distributions of satellite-derived Chla from VIIRS data (c) before the typhoon on 24–26 September, (d) during the typhoon on 27–29 September, and (e) after the typhoon on 30 September to 2 October in 2013.

induced by Typhoon Wutip. This water mass in the top 50 m was slight cooler and saltier after the typhoon than the counterpart before the typhoon. The AEIN also had significant changes in hydrography, particularly temperature, at depths greater than 50 up to 550 m (data below 200 m were not shown). The posttyphoon temperature was warmer than the pretyphoon temperature at depths between 50 and 550 m, indicating strong downwelling over the central and northern parts of the anticyclonic eddy. The occurrence of strong downwelling inside the anticyclonic eddy is consistent with previous findings [Chu *et al.*, 2014].

During the study period, Argo float 5904061 was located inside the AEIN, but at about 110 km to the south of the center of the AEIN (Figures 1 and 4, row C). Figure 7e demonstrates that the MLD decreased from 55 m before the typhoon on 26 September to 45 m after the typhoon on 30 September. In the top mixed layer at this Argo float, the temperature and salinity were vertically uniform before and after the typhoon, and the posttyphoon temperature was lower than the pretyphoon temperature due mainly to intense storm-induced vertical mixing. By comparison, the posttyphoon salinity in the top mixed layer was lower than the pretyphoon salinity observed by this Argo float, due to large rainfall accompanied by Typhoon Wutip (Figure 5b, row B).

Distributions of Chla at the sea surface derived from daily VIIRS data were also affected significantly by Typhoon Wutip, particularly along the storm path (Figures 8c and 8e). Before the typhoon on 24–26 September, the 3 day time-mean sea surface Chla was relatively low and about 0.10 mg m^{-3} over areas with valid data. After the typhoon on 30 September and 2 October, the 3 day time-mean sea surface Chla increased significantly over the western part of the study region, with typical values of about 0.3 mg m^{-3} . Significant changes in the sea surface Chla occurred in the CEIN and OUT on the right of the storm track, where large storm-induced SST cooling occurred (Figure 5, row B). Over the area of Argo float 5904061, the sea surface Chla was relatively low before the typhoon and about 0.07 mg m^{-3} and increased to 0.15 mg m^{-3} after the typhoon. Over the central area of the AEIN, by comparison, the storm-induced changes in the sea surface Chla and SST were small.

Figures 8a and 8b present in situ observations of Chla at locations marked by colored square symbols before the typhoon and by colored circle symbols after the typhoon. The in situ observations are in good agreement with the satellite remote sensing data shown in Figures 8c and 8e. It should be noted that the cruise tracks were about 110 km to the north of the storm track. It is not surprising that in situ observations did not capture the large increases in the sea surface Chla occurred over areas around the storm track shown in Figure 8e.

4. Discussion

In this section, we discuss the temporal and spatial variability of the partial pressure of CO₂ at the sea surface and the air-sea flux of CO₂ over the NSCS during Typhoon Wutip, based on in situ observations and satellite remote sensing data presented in section 3.

4.1. Typhoon-Enhanced pCO_{2,sea} Within a Cyclonic Eddy and Adjacent Waters

Before the passage of Typhoon Wutip on 25–27 September, as shown in Figures 3a and 3b, the observed pCO_{2,sea} along cruise tracks was not strongly correlated with the observed sea surface temperature (SST) and sea surface salinity (SSS), indicating that biological processes played an important role in affecting the spatial variations in observed pCO_{2,sea} along the scientific cruise track at about 18°N. After the passage of the storm on 1–2 October, the observed pCO_{2,sea} was highly correlated with the observed SST ($R^2 = 0.79$, $p < 0.000$) and SSS ($R^2 = 0.73$, $p < 0.000$; Figures 3c and 3d). This high correlation between observed pCO_{2,sea} and observed hydrography at the sea surface after the typhoon suggests that the posttyphoon pCO_{2,sea} was primarily controlled by physical processes such as typhoon-induced mixing and upwelling/downwelling.

Distributions of pCO₂ during the study period were also affected by the large-scale density-driven oceanic circulation over the NSCS. The surface geostrophic circulation over the NSCS during this period had a large-scale anticyclonic eddy (AEIN) over the central NSCS, a small-scale cyclonic eddy (CEIN) to the west of this anticyclonic eddy, and several smaller-size eddies around the AEIN and CEIN. Before the passage of Typhoon Wutip, the pCO_{2,sea} within the CEIN was about 392.92 μatm , which was slightly lower than the value of 393.04 μatm within the water mass surrounding the cyclonic eddy. Our results were consistent with previous findings that upward advection within the cyclonic eddy resulted in the upwelling of deeper cold and CO₂-rich water to the surface, which, together with biological uptake, lead to low pCO_{2,sea} values [Chen *et al.*, 2007; Bond *et al.*, 2011].

After the passage of Typhoon Wutip on 1–2 October, high pCO_{2,sea} ($413.05 \pm 7.56 \mu\text{atm}$) and high air-sea CO₂ flux ($3.30 \pm 0.75 \text{ mmol CO}_2 \text{ m}^{-2} \text{ d}^{-1}$) were observed within the CEIN. It should be noted that the CEIN was the water mass affected directly by Typhoon Wutip. The higher SSS, higher Chla, and lower SST were also observed within the CEIN after the typhoon based on in situ observations (Figures 2 and 8) and satellite remote sensing data (Figure 5, row B), in comparison with the pretyphoon values. As mentioned earlier, the pCO_{2,sea} was highly correlated with SST and SSS after the typhoon. These characteristics and high correlations indicate that cold, salty, and CO₂-rich subsurface waters were mixed with the surface waters within the CEIN. In addition, the decreased MLD within the CEIN during the study period indicates the importance of upwelling in this water mass.

The negative air-sea CO₂ flux is the result of the efflux of deeper water with high pCO_{2,sea} into the surface. Within the CEIN, the 3 day time-mean EPV calculated from satellite wind data was $\sim 5 \times 10^{-5} \text{ m s}^{-1}$ (Figure 4, row B). By assuming the duration is 3 days, this yields an estimation of the wind-driven upwelling of 13 m, which is comparable to the observed decrease of the MLD by about 14 m at Argo float 2901436 within the CEIN (Figure 7c). At this Argo float position, temperature decreased and salinity increased at depths in the top 200 m during a 3 day period on 27–29 September, indicating again the important role of upwelling to the negative air-sea CO₂ flux within the CEIN.

Within the OUT, relatively higher SSS, lower SST, deeper MLD, higher pCO_{2,sea} ($396.97 \pm 3.42 \mu\text{atm}$), and higher air-sea CO₂ flux ($1.71 \pm 0.51 \text{ mmol CO}_2 \text{ m}^{-2} \text{ d}^{-1}$) were observed after the typhoon, in comparison with the pretyphoon conditions. The correlation between SSS and pCO_{2,sea} was significantly positive ($R^2 = 0.40$, Figure 3), and the SST was not correlated with pCO_{2,sea} ($R^2 = 0.02$, Figure 3). These characteristics, together with high correlation between pCO_{2,sea} and SSS, indicate that the deep cold and salty water were mixed and upwelled to the surface within the OUT. The upwelling of high pCO_{2,sea} water into the surface increased the CO₂ efflux from the sea to the atmosphere.

4.2. Decrease in pCO_{2,sea} Within the Anticyclonic Eddy

Within the anticyclonic eddy water mass (AEIN), the posttyphoon pCO_{2,sea} ($383.03 \pm 3.72 \mu\text{atm}$) was lower than the pretyphoon air value ($390.31 \pm 0.50 \mu\text{atm}$). The posttyphoon air-sea CO₂ flux was negative ($-0.11 \pm 0.55 \text{ mmol CO}_2 \text{ m}^{-2} \text{ d}^{-1}$), while the pretyphoon air-sea CO₂ flux was large and positive ($1.51 \pm 0.05 \text{ mmol CO}_2 \text{ m}^{-2} \text{ d}^{-1}$) within the AEIN. Along the cruise track over the northern part of the AEIN, the SST was slightly lower, the SSS was slightly higher, and the MLD was shallower after the typhoon in

comparison with the pretyphoon oceanographic conditions (Figures 2 and 7d), even though a relatively heavy precipitation occurred over this area during the passage of Typhoon Wutip (Figure 5, row A). Within the AEIN after the typhoon, the SSS was highly correlated with $p\text{CO}_{2\text{sea}}$ ($R^2 = 0.73$, Figure 3) and the SST was moderately correlated with $p\text{CO}_{2\text{sea}}$ ($R^2 = 0.32$, Figure 3). These characteristics and posttyphoon high correlations indicate that the cold and salty subsurface water within the AEIN were mixed with the surface water in the top 50 m due to the impact of Typhoon Wutip. Moreover, a large typhoon-induced precipitation introduced additional buoyancy in the surface water and increased the stability of the vertical stratification [Huang and Imberger, 2010], thus inhibiting the vertical mixing and subsequently influencing the $p\text{CO}_{2\text{sea}}$. Based on a simple thermodynamic relationship suggested by Takahashi *et al.* [1993],

$$\frac{\partial p\text{CO}_2 / \partial \text{SST}}{p\text{CO}_2} \cong 0.0423^\circ\text{C}^{-1}, \quad (7)$$

the SST cooling of about -0.56°C (the difference in SST before and after Wutip in the AEIN was about 0.56°C) led to a decrease of $-8.48 \mu\text{atm}$ in $p\text{CO}_{2\text{sea}}$. This estimated decrease is comparable to the observed decrease in $p\text{CO}_{2\text{sea}}$ by about $-7.28 \mu\text{atm}$ (Table 1).

The main processes for the typhoon-induced SST cooling include vertical mixing due to inertial-current resonance and winds, Ekman pumping, and heat loss to the atmosphere [Price, 1981; Huang and Oey, 2015]. Though the air-sea interaction, typhoons draw their energy from warm ocean waters to strengthen its intensification and induced sea surface cooling [Emanuel, 1986; Lin *et al.*, 2009; Tseng *et al.*, 2007; Jaimes and Shay, 2015]. The 3 day time-mean net heat flux at the sea surface within the AEIN changed from a heat gain (about 80.2 W m^{-2}) by the ocean before the typhoon to a heat loss (about -88.2 W m^{-2}) during the typhoon, and to a heat gain (about 46.7 W m^{-2}) after the typhoon (Figure 5, row C). The SST change due to the net heat flux alone (ΔSST_1) can be estimated from [Xie *et al.*, 2010],

$$\Delta\text{SST}_1 = \frac{\Delta t Q_{\text{net}}}{\rho C_p H}, \quad (8)$$

where ρ represents the seawater density, C_p is the specific heat of seawater at constant pressure, H is the mixed layer depth, and Q_{net} is the net heat flux. The estimated SST cooling during the typhoon is about -0.11°C . Since the observed SST cooling within the AEIN during the typhoon was about -0.56°C , the SST cooling due to the wind-induced vertical mixing (and upwelling) was equal to $-0.56 - (-0.11) = -0.45^\circ\text{C}$. As mentioned earlier, the CTD observations at depths greater than 50 m at the center of the AEIN (Figure 7d) suggested occurrence of downwelling within the AEIN, which is consistent with previous findings for anticyclonic eddies [McGillicuddy and Robinson, 1997; Chu *et al.*, 2014]. Therefore, the storm-induced vertical mixing also played a very important role for the observed SST cooling in the top 50 m with the AEIN.

At Argo float 5904061 over the southern part of the AEIN (Figure 7e), the observed temperature and salinity profiles in the vertical (Figure 7e) indicate that the storm-induced intense vertical mixing in the top 50 m and storm-induced large upwelling in the water column less than 500 m (data only show in the upper 200 m). As mentioned earlier, the observed salinity in the top 50 m at this Argo float location decreased by 0.3 psu from 26 to 30 September, due to the heavy rainfall before and during Typhoon Wutip (Figure 5, row A). Based on the analysis above, the upper layer mixing depth within the AEIN was about 50 m. Previous studies indicated that the $p\text{CO}_2$ was constant in the upper 40 m and MLD was 20 m at SEATS station (116°E , 18°N) on 2–7 October 2001 [Tseng *et al.*, 2007, Figure 4]. In other words, the depth of constant $p\text{CO}_2$ was 20 m deeper than the MLD. In this case, the $p\text{CO}_2$ appeared to be uniform in the upper 71 m.

The biological photosynthesis process can also decrease $p\text{CO}_2$ and respiration process can increase $p\text{CO}_2$ [Dai *et al.*, 2009; Krause-Jensen and Sand-Jensen, 1998]. Within the AEIN based on VIIRS images, the Chla was less than 0.1 mg m^{-3} before the typhoon and slightly increased to 0.12 mg m^{-3} after the typhoon (Figure 8). This very small Chla change indicates that biological process may not have much impact on $p\text{CO}_2$ in this case. The $p\text{CO}_2$ change in response to typhoons is ultimately determined by the coupled DIC (CO_2 -rich), TA, temperature and salinity change, and phytoplankton photosynthesis. The temperature was found to be the decisive factor in decreasing $p\text{CO}_2$ in the case of Hurricanes Felix and Frances in the North Atlantic Ocean [Bates *et al.*, 1998; Huang and Imberger, 2010]. By comparison, DIC is the most important factor in increasing $p\text{CO}_2$ in the case of tropical depression in the SCS [Sun *et al.*, 2014]. In this study, the increased $p\text{CO}_{2\text{sea}}$ in

the CEIN and OUT was due to the fact that the CO₂-rich subsurface waters were mixed and upwelled to the surface, while the decreased pCO_{2,sea} in the AEIN was due mainly to SST cooling.

4.3. Impact of Typhoon Wutip on the Local Air-Sea CO₂ Exchange

Before the passage of Typhoon Wutip, the area-averaged air-sea CO₂ flux was about 1.44 ± 0.61 , 1.24 ± 0.38 , and 1.51 ± 0.05 mmol CO₂ m⁻² d⁻¹, respectively, over the CEIN, OUT, and AEIN, indicating that in autumn the NSCS was a regional source for the atmospheric CO₂. Our finding is consistent with previous studies [Zhai *et al.*, 2005, 2013]. Due to the effect of Typhoon Wutip, however, the area-averaged posttyphoon air-sea CO₂ flux over the CEIN and OUT increased to about 3.30 ± 0.75 and 1.71 ± 0.51 mmol CO₂ m⁻² d⁻¹, respectively, which were about 38–130% increases from the pretyphoon values. Within the AEIN, the area-averaged posttyphoon air-sea CO₂ flux was about -0.11 ± 0.55 mmol CO₂ m⁻² d⁻¹, meaning that Typhoon Wutip turned the AEIN from a CO₂ source into a sink. The storm-induced changes in the CO₂ flux within the AEIN during Typhoon Wutip were about $-0.11 - 1.51 = -1.62$ mmol CO₂ m⁻² d⁻¹, which had about 34% changes compared to the average seasonal air-sea CO₂ flux in the northern basin of the SCS (1.2 ± 2.0 mmol CO₂ m⁻² d⁻¹) reported by Zhai *et al.* [2013]. The storm-induced decrease in the air-sea CO₂ flux during Typhoon Wutip was only about 1.28 (before) $- 1.31$ (after) = -0.03 mmol CO₂ m⁻² d⁻¹, indicating that Typhoon Wutip had a minor impact on the air-sea CO₂ flux.

It should be noted that the impact on the air-sea CO₂ flux by a typhoon is a complicated process. High winds accompanied by a typhoon enhance the gas transfer velocity, and then increase the air-sea CO₂ flux. Previous studies demonstrated that the increase in the CO₂ efflux was mainly caused by increases in the wind speed for Typhoons T9711 and T9713 [Nemoto *et al.*, 2009] and Typhoon Felix [Bates *et al.*, 1998]. Wada *et al.* [2013] reported that the decrease in pCO_{2,air} explained about 40% of the air-sea CO₂ flux. Most of previous studies found the variation of pCO_{2,sea} is the main reason for the change in the air-sea CO₂ flux. Previous studies also suggested that the typhoon-induced SST cooling was the dominant reason for the decrease of pCO_{2,sea} [Bates *et al.*, 1998; Huang and Imberger, 2010]. The typhoon-uplifted deeper CO₂-rich water, however, could increase pCO_{2,sea} [Sun *et al.*, 2014]. An increase in the CO₂ efflux from the ocean to atmosphere caused by typhoons was observed [Bates *et al.*, 1998; Perrie *et al.*, 2004; Nemoto *et al.*, 2009]. A tropical depression was found to transform a carbon sink area to carbon source in the SCS [Sun *et al.*, 2014]. In this study, we documented two different responses after the passage of Typhoon Wutip: high pCO_{2,sea} with a high efflux of CO₂ and low pCO_{2,sea} with a low influx of CO₂. Our results are consistent with the results reported by Levy *et al.* [2012], who found that the typhoon-generated CO₂ flux depended on the CO₂ conditions at the time of the typhoon's passage.

The enhanced efflux from the ocean to atmosphere over the CEIN and OUT can be explained by two factors: (1) the shallow MLD in the preexisted cyclonic eddy that made relatively easy to bring subsurface waters to the surface by a typhoon and (2) strong vertical mixing generated by inertial-current resonance and intense winds accompanied by a typhoon. Over the AEIN, the efflux transformed to influx from the ocean to atmosphere can be explained by (1) the sea surface cooling which induced by typhoon drew heat energy and (2) intense precipitation brought by typhoon. More than 130 mm rain diluted SSS from about 33.32 to 30.04 (Argo float: 5904061) which decreased surface pCO_{2,sea}.

5. Summary and Conclusions

In this study, we examined the typhoon-induced changes in the partial pressure of CO₂ at the sea surface (pCO_{2,sea}) and the air-sea CO₂ flux during Category 2 Typhoon Wutip over the northern South China Sea (NSCS). Several types of in situ oceanographic observations and satellite remote sensing data were used in the analysis. Typhoon Wutip generated extreme marine conditions, such as intense wind-driven currents, strong vertical mixing, large ocean waves, and Wind Pump effect, over the NSCS during a 3 day period on 27–29 September.

The typhoon-induced air-sea CO₂ flux (F_{CO_2}) was quantified during Typhoon Wutip over three different water masses in the NSCS: a large-size anticyclonic eddy water (AEIN) over the central area of the NSCS, a small-size cyclonic eddy water (CEIN), and water mass surrounding the cyclonic eddy (OUT). Different mechanisms were involved for the observed changes in pCO_{2,sea} and air-sea CO₂ flux over different water masses.

Over the CEIN and OUT, an increase of about 38–130% in the CO₂ flux from the ocean to the air was explained by the entraining/mixing CO₂-rich subsurface water due to a preexisting shallow mixed layer depth (20 m) and strong vertical mixing generated by inertial-current resonance and intense winds accompanied by Typhoon Wutip. The high pCO_{2,sea} after Wutip in the CEIN and OUT can be explained by strong entraining/mixing and uplifting of CO₂-rich subsurface water due to the preexisting shallow mixed-layer depth (20 m) before the typhoon and intense winds accompanied by Typhoon Wutip.

Over the AEIN, the CO₂ flux from the ocean to the air was changed into the flux from the air to the ocean during the study period. This change was primarily accounted for by the storm-induced SST cooling and a relatively thick mixed-layer depth (about 45 m) that reduced the subsurface water entrain/mix to surface. Intense rainfall brought by Typhoon Wutip strengthened the water column stratification in the vertical, thereby reducing the subsurface water entrainment. The low pCO_{2,sea} after Wutip in the AEIN was associated with strong sea surface cooling as a result of intense vertical mixing in the surface layer and strong upwelling, both of which were generated by Typhoon Wutip. It should be noted that downwelling occurred over the central area of the AEIN, which was not generated directly by Typhoon Wutip.

Our results demonstrated that Typhoon Wutip generated large spatial variations in the pCO_{2,sea}, by increasing the CO₂ efflux within the CEIN and OUT and transforming CO₂ efflux into CO₂ influx in the AEIN. Our results also demonstrated that the impact of Typhoon Wutip on the local air-sea CO₂ flux over the NSCS was largely determined by the oceanographic conditions during the passage of the typhoon. It should be noted that the typhoon-induced changes in pCO_{2,sea} and F_{CO2} were estimated based on in situ observations made along the cruise tracks, which were about 110 km away from the typhoon path over the NSCS. It should also be noted that analyses of in situ observations presented in this paper were made based mainly on the local processes such as vertical mixing and upwelling/downwelling. The other processes may also play an important role. *Huang and Oey* [2015], for an example, demonstrated that the right-biased enhanced phytoplankton bloom in the wake of a tropical cyclone can also be caused by decreased turbulence due to restratification by recirculation cells produced on the right side, rightward shift of cool isotherms, and spin-up of a subsurface jet in the northern hemisphere. Our future studies will include an examination of responses of pCO_{2,sea} and F_{CO2} to the typhoon along the typhoon path, using three-dimensional fields of circulation and hydrography to be simulated by a numerical ocean circulation model forced by atmospheric forcing associated with typhoon Wutip.

Acknowledgments

This study was funded by Key Project (41430968) of the National Natural Sciences Foundation of China and the Key Project (2015H505) of Collaborative Innovation Centre for 21st Century Mari-time Silk Road Program (GDUFS). J.S. was supported by NSERC, MEOPAR, and LTO Overseas Visiting Fellowship Program (LTO-OVFP 1601). In situ data were obtained during the South China Sea Research Cruise, R/V Shiyan 3, and those data available online from the South China Sea Ocean Database (<http://www.scsio.csdb.cn/>) and the National Earth System Science Data Sharing Infrastructure (<http://ocean.geodata.cn/>). Argo floats data were collected and made freely available by the International Argo Program and the national programs that contribute to it (<http://www.argo.ucsd.edu>, <http://argo.jcommops.org>). The Argo Program is part of the Global Ocean Observing System.

References

- Bates, N. R., A. H. Knap, and A. F. Michaels (1998), Contribution of hurricanes to local and global estimates of air-sea exchange of CO₂, *Nature*, 395(6697), 58–61, doi:10.1038/25703.
- Bond, N. A., M. F. Cronin, C. Sabine, Y. Kawai, H. Ichikawa, P. Freitag, and K. Ronnholm (2011), Upper ocean response to Typhoon Choi-Wan as measured by the Kuroshio Extension Observatory mooring, *J. Geophys. Res.*, 116, C02031, doi:10.1029/2010JC006548.
- Chen, F. Z., W. J. Cai, C. Benitez-Nelson, and Y. C. Wang (2007), Sea surface pCO₂-SST relationships across a cold-core cyclonic eddy: Implications for understanding regional variability and air-sea gas exchange, *Geophys. Res. Lett.*, 34, L10603, doi:10.1029/2006GL028058.
- Chu, X. Q., H. J. Xue, Y. Q. Qi, G. X. Chen, Q. W. Mao, D. X. Wang, and F. Chai (2014), An exceptional anticyclonic eddy in the South China Sea in 2010, *J. Geophys. Res. Oceans*, 119, 881–897, doi:10.1002/2013JC009314.
- Dai, M. H., Z. Lu, W. Zhai, B. Chen, Z. Cao, K. Zhou, W. J. Cai, and C.-T. A. Chen (2009), Diurnal variations of surface seawater pCO₂ in contrasting coastal environments, *Limnol. Oceanogr.*, 54(3), 735–745.
- Emanuel, K. A. (1986), An air-sea interaction theory for tropical cyclones. Part I: Steady-state maintenance, *J. Atmos. Sci.*, 43(6), 585–605.
- Hood, E., R. Wanninkhof, and L. Merlivat (2001), Short timescale variations of fCO₂ in a North Atlantic warm-core eddy: Results from the Gas-Ex 98 carbon interface ocean atmosphere (CARIOCA) buoy data, *J. Geophys. Res.*, 106(C2), 2561–2572, doi:10.1029/1999JC000278.
- Huang, P., and J. Imberger (2010), Variation of pCO₂ in ocean surface water in response to the passage of a hurricane, *J. Geophys. Res.*, 115, C10024, doi:10.1029/2010JC006185.
- Huang, S.-M., and L.-Y. Oey (2015), Right-side cooling and phytoplankton bloom in the wake of a tropical cyclone, *J. Geophys. Res. Oceans*, 120, 5735–5748, doi:10.1002/2015JC010896.
- Hung, C.-C., G.-C. Gong, W.-C. Chou, C.-C. Chung, M.-A. Lee, Y. Chang, H.-Y. Chen, S.-J. Huang, Y. Yang, and W.-R. Yang (2010), The effect of typhoon on particulate organic carbon flux in the southern East China Sea, *Biogeosciences*, 7(10), 3007–3018, doi:10.5194/bg-7-3007-2010.
- Jaimes, B., and L. K. Shay (2015), Enhanced wind-driven downwelling flow in warm oceanic eddy features during the intensification of tropical cyclone Isaac (2012): Observations and theory, *J. Phys. Oceanogr.*, 45(6), 1667–1689.
- Jarosz, E., D. A. Mitchell, D. W. Wang, and W. J. Teague (2007), Bottom-up determination of air-sea momentum exchange under a major tropical cyclone, *Science*, 315(5819), 1707–1709, doi:10.1126/science.1136466.
- Knutson, T. R., J. L. McBride, J. Chan, K. Emanuel, G. Holland, C. Landsea, I. Held, J. P. Kossin, A. Srivastava, and M. Sugi (2010), Tropical cyclones and climate change, *Nat. Geosci.*, 3(3), 157–163, doi:10.1038/NNGEO779.
- Ko, D. S., S.-Y. Chao, C.-C. Wu, and I. I. Lin (2014), Impacts of Typhoon Megi (2010) on the South China Sea, *J. Geophys. Res. Oceans*, 119, 4474–4489, doi:10.1002/2013JC009785.
- Koch, J., G. A. McKinley, V. Bennington, and D. Ullman (2009), Do hurricanes cause significant interannual variability in the air-sea CO₂ flux of the subtropical North Atlantic?, *Geophys. Res. Lett.*, 36, L07606, doi:10.1029/2009GL037553.

- Krause-Jensen, D., and K. Sand-Jensen (1998), Light attenuation and photosynthesis of aquatic plant communities, *Limnol. Oceanogr.*, *43*(3), 396–407, doi:10.4319/lo.1998.43.3.0396.
- Le Quéré, C., M. R. Raupach, J. G. Canadell, G. Marland, L. Bopp, P. Ciais, T. J. Conway, S. C. Doney, R. A. Feely, and P. Foster (2009), Trends in the sources and sinks of carbon dioxide, *Nat. Geosci.*, *2*(12), 831–836, doi:10.1038/ngeo689.
- Levy, M., M. Lengaigne, L. Bopp, E. M. Vincent, G. Madec, C. Éthé, D. Kumar, and V. Sarma (2012), Contribution of tropical cyclones to the air-sea CO₂ flux: A global view, *Global Biogeochem. Cycles*, *26*, GB2001, doi:10.1029/2011GB004145.
- Lin, I. I., C. H. Chen, I. F. Pun, W. T. Liu, and C. C. Wu (2009), Warm ocean anomaly, air sea fluxes, and the rapid intensification of tropical cyclone Nargis (2008), *Geophys. Res. Lett.*, *36*, L03817, doi:10.1029/2008GL035815.
- Lonfat, M., F. D. Marks Jr., and S. S. Chen (2004), Precipitation distribution in tropical cyclones using the tropical rainfall measuring mission (TRMM) microwave imager: A global perspective, *Mon. Weather Rev.*, *132*(7), 1645–1660.
- McGillicuddy, D., and A. Robinson (1997), Eddy-induced nutrient supply and new production in the Sargasso Sea, *Deep Sea Res., Part I*, *44*(8), 1427–1450, doi:10.1016/S0967-0637(97)00024-1.
- Monterey, G., and S. Levitus (1997), *Climatological Cycle of Mixed Layer Depth in the World Ocean*, 5 pp., U.S. Govt. Print. Off., Washington, D. C.
- Nemoto, K., T. Midorikawa, A. Wada, K. Ogawa, S. Takatani, H. Kimoto, M. Ishii, and H. Inoue (2009), Continuous observations of atmospheric and oceanic CO₂ using a moored buoy in the East China Sea: Variations during the passage of typhoons, *Deep Sea Res., Part II*, *56*(8–10), 542–553, doi:10.1016/j.dsr2.2008.12.015.
- Perrie, W., W. Zhang, X. Ren, Z. Long, and J. Hare (2004), The role of midlatitude storms on air-sea exchange of CO₂, *Geophys. Res. Lett.*, *31*, L09306, doi:10.1029/2003GL019212.
- Pierrot, D., C. Neill, K. Sullivan, R. Castle, R. Wanninkhof, H. Lüger, J. Truls, O. Are, A. F. Richard, and C. E. Cosca (2009), Recommendations for autonomous underway pCO₂ measuring systems and data-reduction routines, *Deep Sea Res., Part II*, *56*(8), 512–522, doi:10.1016/j.dsr2.2008.12.005.
- Price, J. F. (1981), Upper ocean response to a hurricane, *J. Phys. Oceanogr.*, *11*(2), 153–175, doi:10.1175/1520-0485(1981)011.
- Sarma, V., H. Delabehra, P. Sudharani, R. Remya, J. Patil, and D. Desai (2015), Variations in the inorganic carbon components in the thermal fronts during winter in the northeastern Arabian Sea, *Mar. Chem.*, *169*, 16–22, doi:10.1016/j.marchem.2014.12.009.
- Sheng, J., X. Zhai, and R. J. Greatbatch (2006), Numerical study of the storm-induced circulation on the Scotian Shelf during Hurricane Juan using a nested-grid ocean model, *Prog. Oceanogr.*, *70*(2), 233–254, doi:10.1016/j.pocean.2005.07.007.
- Shih, Y. Y., J. S. Hsieh, G. C. Gong, C. C. Hung, W. C. Chou, M. A. Lee, K. S. Chen, M. H. Chen, and C. R. Wu (2013), Field observations of changes in SST, chlorophyll and POC flux in the southern East China Sea before and after the passage of Typhoon Jangmi, *Terr. Atmos. Oceanic Sci.*, *24*(5), 899–910, doi:10.3319/TAO.2013.05.23.01(Oc).
- Sun, Q. Y., D. L. Tang, L. Legendre, and P. Shi (2014), Enhanced sea-air CO₂ exchange influenced by a tropical depression in the South China Sea, *J. Geophys. Res. Oceans*, *119*, 6792–6804, doi:10.1002/2014JC010131.
- Takahashi, T., J. Olafsson, J. G. Goddard, D. W. Chipman, and S. C. Sutherland (1993), Seasonal-variation of CO₂ and nutrients in the highlatitude surface oceans—A comparative-study, *Global Biogeochem. Cycles*, *7*(4), 843–878, doi:10.1029/93GB02263.
- Takahashi, T., et al. (2002), Global sea-air CO₂ flux based on climatological surface ocean pCO₂, and seasonal biological and temperature effects, *Deep Sea Res., Part II*, *49*(9), 1601–1622, doi:10.1016/S0967-0645(02)00003-6.
- Tseng, C.-M., G. Wong, W.-C. Chou, B.-S. Lee, D.-D. Sheu, and K.-K. Liu (2007), Temporal variations in the carbonate system in the upper layer at the SEATS station, *Deep Sea Res., Part II*, *54*(14), 1448–1468, doi:10.1016/j.dsr2.2007.05.003.
- Turk, D., C. J. Zappa, C. S. Meinen, J. R. Christian, D. T. Ho, A. G. Dickson, and W. R. McGillis (2010), Rain impacts on CO₂ exchange in the western equatorial Pacific Ocean, *Geophys. Res. Lett.*, *37*, L23610, doi:10.1029/2010GL045520.
- Wada A, M. F. Cronin, A. J. Sutton, Y. Kawai, and M. Ishii (2013), Numerical simulations of oceanic pCO₂ variations and interactions between Typhoon Choi-Wan (0914) and the ocean, *J. Geophys. Res.*, *118*, 2667–2684, doi:10.1002/jgrc.20203.
- Wanninkhof, R. (1992), Relationship between wind speed and gas exchange over the ocean, *J. Geophys. Res.*, *97*(C5), 7373–7382, doi:10.1029/92JC00188.
- Wanninkhof, R., A. Olsen, and J. Triñanes (2007), Air-sea CO₂ fluxes in the Caribbean Sea from 2002–2004, *J. Mar. Syst.*, *66*(1–4), 272–284, doi:10.1016/j.jmarsys.2006.11.014.
- Wanninkhof, R., W. E. Asher, D. T. Ho, C. Sweeney, and W. R. McGillis (2009), Advances in quantifying air-sea gas exchange and environmental forcing, *Annu. Rev. Mar. Sci.*, *1*, 213–244, doi:10.1146/annurev.marine.010908.163742.
- Weiss, R. F. (1974), Carbon dioxide in water and seawater: The solubility of a non-ideal gas, *Mar. Chem.*, *2*(3), 203–215, doi:10.1016/0304-4203(74)90015-2.
- Xie, S. P., C. Deser, G. A. Vecchi, J. Ma, H. Y. Teng, and A. T. Wittenberg (2010), Global warming pattern formation: Sea surface temperature and rainfall, *J. Clim.*, *23*(4), 966–986.
- Ye, H., Y. Sui, D. Tang, and Y. Afanasyev (2013), A subsurface chlorophyll a bloom induced by typhoon in the South China Sea, *J. Mar. Syst.*, *128*, 138–145, doi:10.1016/j.jmarsys.2013.04.010.
- Yu, J., D. Tang, G. Chen, Y. Li, Z. Huang, and S. Wang (2014), The positive effects of typhoons on the fish CPUE in the South China Sea, *Cont. Shelf Res.*, *84*, 1–12, doi:10.1016/j.csr.2014.04.025.
- Zhai, W., M. Dai, W. J. Cai, Y. Wang, and Z. Wang (2005), High partial pressure of CO₂ and its maintaining mechanism in a subtropical estuary: The Pearl River estuary, China, *Mar. Chem.*, *93*(1), 21–32, doi:10.1016/j.marchem.2004.07.003.
- Zhai, W. D., M. H. Dai, B. S. Chen, X. H. Guo, Q. Li, S. L. Shang, C. Y. Zhang, W. J. Cai, and D. X. Wang (2013), Seasonal variations of sea-air CO₂ fluxes in the largest tropical marginal sea (South China Sea) based on multiple-year underway measurements, *Biogeosciences*, *10*(11), 7775–7791, doi:10.5194/bg-10-7775-2013.
- Zhao, H., D. Tang, and D. Wang (2009), Phytoplankton blooms near the Pearl River Estuary induced by Typhoon Nuri, *J. Geophys. Res.*, *114*, C12027, doi:10.1029/2009JC005384.